

INVESTIGATION OF Li-Al-Si-O₄ CERAMIC AS SOLID ELECTROLYTE SYNTHESIZED BY SOLID STATE METHOD

Thesis submitted

In partial fulfilment of the requirements for the

Degree of

MASTER OF SCIENCE

in

APPLIED PHYSICS

Submitted By:

PARUL SOLANKI

(23/MSCPHY/38)

&

AYUSHI SHARMA

(23/MSCPHY/90)

Under the supervision of

DR. AMRISH K. PANWAR

(Associate Professor)



Department of Applied Physics

DELHI TECHNOLOGICAL UNIVERSITY

(Formerly Delhi College of Engineering)

Shahbad Daultapur, Main Bawana Road, Delhi-110042, India.

June 2025

CANDIDATE'S DECLARATION

We, **PARUL SOLANKI**, Roll No. **23/MSCPHY/38** and **AYUSHI SHARMA**, Roll No. **23/MSCPHY/90** hereby certify that the work which is presented in the thesis entitled "**Investigation of Li-Al-Si-O₄ ceramic as solid electrolyte synthesized by solid state method**" in partial fulfilment of the requirement for the award of the Degree of Master of Science in Physics submitted in the Department of Applied Physics, Delhi Technological University, Delhi is an authentic record of our own work carried out during the period from August 2024 to June 2025 under the supervision of **Dr. Amrish K. Panwar**.

The matter presented in the thesis has not been submitted by me for the award of any other degree of this or any other institute. The work has been Communicated in a peer reviewed Scopus indexed conference with the following details:

Title of the Paper: Structural and dielectric properties investigation of Li-Al-Si-O₄ ceramic solid electrolyte synthesized by solid state method

Author names: Ayushi Sharma, Parul Solanki, Sharad Singh Jadaun and Dr. Amrish K. Panwar

Name of Conference: International Conference on Advanced Materials for Sustainable Future (ICAMSF-2025).Conference

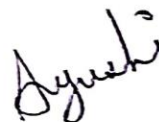
Dates with the venue: 27th-29nd March, 2025, Chitkara University Panjab, India

Conference Registered: Yes

Status of paper (Accepted/Published/Communicated): Communicated



Parul Solanki
(23/MSCPHY/38)




Ayushi Sharma
(23/MSCPHY/90)

SUPERVISOR CERTIFICATE

To the best of my knowledge, the above work has not been submitted in part or full for any Degree or Diploma to this University or elsewhere. I, further certify that the publication and indexing information given by the students is correct.

Place: Delhi
Date: 09/06/2025


Dr. Amrish K. Panwar
(Supervisor) 09.06.2025

ACKNOWLEDGEMENT

Initially, we express our gratitude towards our supervisor **Dr. Amrish K. Panwar** for granting us the privilege to engage in research work within his esteemed Lithium-Ion Battery Technology Lab. The accomplishment of this work was made feasible through his indispensable guidance and unwavering assistance. Appreciation is extended for his valuable time, feedback, and recommendations. We greatly appreciate his patience in revising manuscripts and sharing his knowledge with us. The methodology he employed in scientific exploration sustained the enthusiasm for research throughout this thesis. We would like to thank Mr. Sharad Singh Jadaun, Mr. Naveen and Mr. Puneet Ph.D. scholars of our lab and our senior for their guidance, suggestions, group discussions and to provide us healthy environment throughout the research work. Gratitude is also owed to all the faculty members, our batchmates, and members of the Department of Applied Physics at Delhi Technological University for their invaluable suggestions and support. We wish to express our thanks to our parents for their enduring encouragement and unwavering belief in our capabilities.

ABSTRACT

The All Solid State Batteries (ASSBs) are recognized as the promising systems for storing energy with overcoming safety issues existing conventional liquid electrolyte-based Li/Na ion rechargeable batteries and also provide high energy density. The solid-state electrolytes (SSEs), are the most critical component of ASSBs. It leads to the future battery research and development. Since, the traditional Li-ion batteries have critical safety issues due to highly flammable liquid electrolytes or thermally instability of polymer electrolytes. Whereas, the ceramic based solid-state electrolyte shows high thermal stability, good ionic conductivity. LiAlSiO_4 (LASO) ceramics have been demonstrated to be a fast Li^+ ion conductor and is cost effective as the element aluminum and silicon are cheaper and abundantly available on the earth, better electrochemical performance and low-cost material open up new possibilities for ceramic based solid-state batteries for commercialization. Herein, LASO ceramic solid electrolyte has been synthesized using the conventional solid-state reaction method. Thermogravimetric analysis (TGA) has been conducted to assess thermal stability of developed SSE. X-ray diffraction (XRD) is employed to confirm the formation of proper crystal structure. The average crystallite size of LASO has been estimated from the XRD pattern by Scherer's formula and W-H plot using prominent XRD peaks. Scanning electron microscopy (SEM) characterization is performed for micro structural and surface morphological analysis of the material. Furthermore, Impedance spectroscopy (IS) has been performed to analyze the ionic conductivity and dielectric properties of SSEs.

Keywords: Solid state battery, Ceramic solid electrolyte, LASO, Ionic conductivity.

TABLE OF CONTENT

● Declaration	ii
● Acknowledgement	iii
● Abstract	iv
● List of Contents	v
● List of Figures	vi
● Abbreviations	vii
1. Introduction and Literature review	1
1.1. Introduction	1
1.2. History of Batteries	2
1.3. Components of Battery	4
1.4. Types of Battery	5
1.5. Working Principle of Battery	6
2. Electrolytes	8
2.1. Types of Electrolytes	8
2.2. LASO A Solid Electrolyte	10
2.3. Objectives of Research Work	10
3. Synthesis and Characterization	11
3.1. Solid State Reaction	11
3.2. Material Synthesis	11
3.3. Material Characterization	12
3.4. X-Ray Diffraction	13
3.5. Scanning Electron Microscope	14
3.6. Thermogravimetric Analysis	16
3.7. Impedance Spectroscopy	18
4. Results and Discussion	21
4.1. Theoretical Analysis of LASO	21
4.2. TGA and DSC Analysis	22
4.3. XRD Analysis	23
4.4. Morphological Analysis	28
4.5. Dielectric Analysis	29
6. Summary and Conclusions	36
Reference	37
Plagiarism Report	40
Conference Record	41

LIST OF FIGURES

Figure 1.1: Electrical energy generation from a "galvanic cell"

Figure 1.2: Discharging and charging of battery.

Figure 3.1: Schematic representation of preparation of LASO electrolyte pellet.

Figure 3.2: Geometric conditions for diffraction from lattice planes.

Figure 3.3: Schematic diagram of the SEM setup illustrating major components.

Figure 4.1: Representation of Crystal structures of LiAlSiO_4 (using VESTA)

Figure 4.2: TGA/DSC curve of hand-grinded sample of LASO

Figure 4.3: XRD pattern of LASO calcinated at different temperatures.

Figure 4.4(a): Temperature versus the LASO SE's average grain size(nm).

Figure 4.4(b): Temperature versus the $d_{(102)}$ plane spacing plot of LASO SEs

Figure 4.5: W-H plot of LASO calcinated at 1000 °C.

Figure 4.6: SEM images of LASO calcinated at 1000° C at the different magnification. Figure

4.7: The curve between real part of permittivity vs frequency of the sample LASO.

Figure 4.7(b): The plot between imaginary part of permittivity vs frequency of the LASO.

Figure 4.8: (a) The curve between real part of impedance vs frequency of the sample LASO.

Figure 4.8: (b) The curve between imaginary part of impedance vs frequency of the sample LASO.

Figure 4.9: (a)Nyquist representation of LASO specimen across thermal conditions from 90°C to 140°C.

Figure 4.9: (b) Nyquist representation of LASO specimen with magnified view, thermal conditions from 90°C to 140°C.

Figure 4.10: Arrhenius plot of ionic conductivity of LASO sample.

Figure 4.11: Arrhenius plot of relaxation time versus temperature for sample LASO

LIST OF SYMBOLS AND ABBREVIATIONS

S. No.	Acronym/Symbol	Full Form
1.	OCV	Open circuit voltage
2.	CCV	Closed circuit voltage
3.	Ah	Ampere hours
4.	RC	Reserve capacity
5.	Li-ion	Lithium ion
6.	SSE	Solid state electrolyte
7.	ESW	Electrochemical stability window
8.	EIS	Electrochemical impedance spectroscopy
9.	XRD	X-ray diffraction
10.	SEM	Scanning electron microscopy
11.	EDS	Energy dispersive spectrometer
12.	TGA	Thermogravimetrics analysis
13.	DSC	Differential scanning calorimetry
14.	IS	Impedance spectroscopy
15.	NTCR	Negative temperature coefficient of resistance
16.	LASO	Lithium aluminium silicon oxide

1

INTRODUCTION AND LITERATURE REVIEW

1.1 INTRODUCTION

The development of alternative energy sources and efficient energy storage technologies is crucial to addressing the pressing global energy demands and the environmental issues related to the usage of fossil fuels. Reducing greenhouse gas emissions, accelerating the transition to a low-carbon society, and achieving global energy independence all depend on these technologies. Developing sustainable and reasonably priced energy storage devices that can effectively harvest energy from renewable sources like solar and wind power is one of the most promising approaches. At present, there is only a minor portion of the world's power capacity stored. Nevertheless, the estimates indicate that by 2050 energy storage capacity must considerably rise to assist in restricting global warming to under 2°C and facilitate climate resilience action. To make this happen, new strategies are needed to speed up the growth in adopting clean energy technologies and intensifying access to renewable energy. One of the biggest challenges of the 21st century is powering the world with clean, low-cost, sustainable, and abundant energy. Solar energy technologies solar photovoltaics (PV) and solar thermal systems in particular are likely to have a major role in this shift, providing pragmatic and scalable solutions. Renewable energy sources compared to fossil fuels are likely to provide greater long-term benefits because of their sustainability and declining costs. As much as these systems have their benefits, they have numerous challenges to large-scale deployment, including high capital expenditures, low policy incentives, and technical constraints. In contrast to traditional generation sources, energy storage technologies are not properly compensated for the grid services and operational advantages they can offer. However, energy storage is an essential function in stabilizing the energy system by storing excess energy when renewable generation is high and releasing it when generation is low. This serves to reduce the variable nature of renewables and result in a more stable supply of energy. Over the past several years, world electricity generation has increased significantly. As of 2012, the gross annual electricity output stood at over 22,200 TWh, with fossil fuels coal, natural gas, and oil—accounting for approximately 70% of the installed capacity [1]. Fossil fuel power plants have traditionally

provided grid stability through managing supply and demand. The energy systems of the future, however, are to decrease the use of fossil fuels, which are finite and inherently environmental in their impact [2,3]. Accordingly, the transition to renewable energy sources is at the heart of lowering carbon dioxide emissions. However, most renewable energy sources are naturally variable and intermittent in character, so strong energy storage technologies are needed to provide for maintaining grid balance and reliability [1]. Improvements in recent battery technologies have introduced a number of advancements from previous generations such as increased energy and power density, longer life, and improved safety characteristics [4]. Battery Energy Storage Systems (BESS) enable the use of renewable energy more effectively by providing a backup power supply, mitigating use of the electrical grid, decreasing carbon footprints, and providing long-term economic benefits.

1.2 HISTORY OF BATTERY

Alessandro Volta created the "electric pistol" as the first practical application of static electricity. He considered enabling long-distance communication, although just one Boolean bit. A wooden pole-supported iron wire intended to be extended from Como to Milan, Italy. The line would terminate in a jar that held methane gas. An electrical spark would be transmitted through wire to explode the jar in order to signal a coded event. When some fluids were used as conductors, Volta discovered in 1800 that they could create a constant flow of electricity. This idea led to development of the first voltaic cell, or battery, as it is more often known. Further investigation showed to Volta that stacking voltaic cells on top of one another would increase voltage [5].

William Cruickshank created the first electric battery that could be produced in large quantities in 1802. He assembled equal-sized square copper and zinc sheets into a long, rectangular wooden box, soldering them together. The metal plates were secured in place by grooves in the box. The electrolyte, or diluted acid, was then placed inside the sealed box. This was similar to the flooded battery that we still have in our possession [5].



Fig.1.1 Electrical energy generation from a "galvanic cell" constructed through an alternating arrangement of two distinct metals (zinc and silver discs) isolated by a fabric immersed in a sodium chloride electrolyte

English scientist John F. Daniell created a better battery in 1836 that produced more consistent current than previous attempts to store electrical energy. Lead-acid based rechargeable battery technology was invented by Gaston Planté in 1859 and is still in use today. All batteries were primary up to that point, which meant they couldn't be reused [6].

The nickel-cadmium (Ni-Cd) battery was created in 1899 by Swedish inventor Waldmar Jungner. Nickel served as positive electrode (cathode), while cadmium served as negative electrode (anode). After switching from cadmium to iron two years later, Thomas Edison named this battery nickel-iron (Ni-Fe). A low specific energy, poor low-temperature performance, and excessive self-discharge hampered the nickel iron battery's success. The majority of current research efforts are focused on enhancing lithium-based systems, which were initially brought to market by Sony in 1991. Li-ion batteries are utilised for electric cars and satellites in addition to powering computers, digital cameras, medical equipment, power tools, and mobile phones. Among the many advantages

of the battery are its high specific energy, ease of charging, low maintenance requirements, and environmental friendliness [7].

1.3 BATTERY BASICS

DEFINITION AND COMPONENTS:-

An electrochemical battery consists of three primary elements: a cathode, an anode, and an electrolyte, which supports the chemical reactions. At charging, positive ions are built up at the interface between the cathode and the electrolyte. This leads to electrons moving to the cathode, resulting in a voltage difference across the cathode and anode. As the battery drains, current moves from the positive cathode, through an external load, and back to the negative anode. In the case of charging, this current is reversed.

A battery works in two different ways. One is the outer electric circuit, whereby electrons move to energize a device that is attached. The other is the inner ionic pathway, whereby ions migrate between electrodes via a separator. The separator is an electron barrier but a passageway for ions electrically charged atoms that have lost or gained electrons thereby ensuring electrical equilibrium in the cell while physically and electrically separating the electrodes.

Anode and Cathode

In a battery, the anode is the electrode from which electrons are emitted when discharging and the cathode is the electrode to which they are received. At this time, the anode is charged negative and the cathode positive. This appears to contradict the common definition where the anode is normally the terminal where current is coming into a device. That definition is true of systems such as vacuum tubes, diodes, or batteries on the way to being charged. But in battery discharge when the battery is delivering power the direction of electron flow makes the anode negative. Because a battery acts as a source of electrical energy on discharge, the anode is always referred to as negative in this usage.

Electrolyte and Separator

Ion movement within a battery is enabled by the electrolyte, which acts as a chemical activator. In flooded battery systems, the electrolyte flows freely between the electrodes. In contrast, sealed

batteries typically contain the electrolyte in a moistened form absorbed into the separator. The separator plays a critical role by physically isolating the anode from the cathode—it blocks the flow of electrons while permitting the passage of ions.

1.4 TYPES OF BATTERY

Batteries are classified on the basis of many parameters like their chemistry, shape, size, or application. The two main types are:

Primary Batteries

Secondary Batteries

Primary Batteries

Primary batteries are single-use power sources and are non-rechargeable. They find special applications where recharge is impossible or not practical, for example, military exercises, emergency rescue operations, handling wildfires, and other remote or time-sensitive operations. Primary batteries are standardized by IEC 60086 standards and are applied in applications such as pacemakers, tire pressure monitors, smart meters, mining machines, animal tracking systems, navigation beacons, watches, remote controls, electronic keys, and children's toys.

Primary batteries are prized for their high specific energy, long storage life, and immediate readiness to use, and are best suited for storage and shipment to remote areas. They will still work even after decades of storage and are generally environmentally safe when disposed of appropriately. Types of primary batteries are Zinc-Carbon, Alkaline Battery, Lithium Iron Disulfide (Li-FeS₂).

Secondary battery

When current is passed in the opposite direction of discharge, a secondary cell or battery can be recharged to its pre-discharge condition. These are also called rechargeable batteries. Even after they have been fully depleted, secondary batteries may be recharged and used again. Secondary batteries must be carefully selected for their intended use, they are better for the environment, less

expensive, and often deliver more power than disposable batteries. The most commonly used rechargeable battery types are lead acid, NiCd, NiMH, and Li-ion.

1.5 WORKING PRINCIPLE OF BATTERY

A standard lithium-ion (Li-ion) battery consists of four basic components: the cathode, anode, electrolyte, and separator. The cathode and anode are the two electrodes of the battery with different chemical potentials, and their values decide the open-circuit voltage of the cell. The

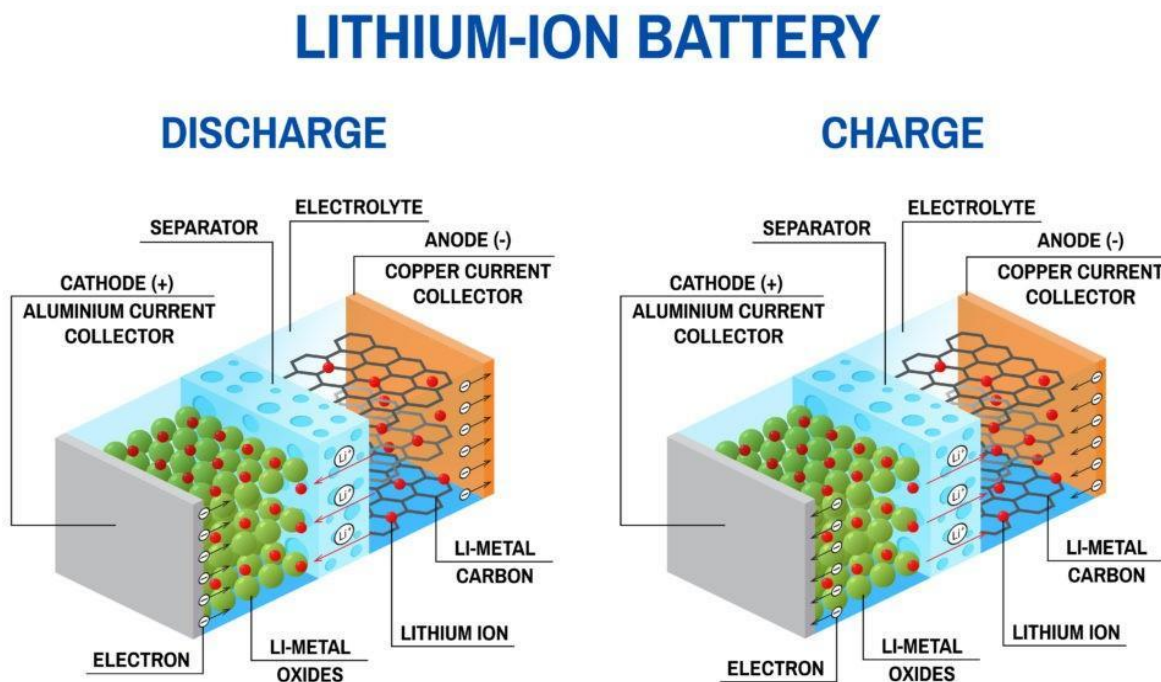


Figure1.2: Discharging and charging of battery.

separator, though inert, plays a crucial role of physically isolating the two electrodes to prevent the short circuit. The electrolyte carries the lithium ions between the electrodes during charge-discharge operations. As a battery is connected to an external circuit, electrons from the anode (negative electrode) flow towards the cathode (positive electrode), resulting in an electric current

due to the potential difference. Along with it, lithium ions migrate through the electrolyte in the same direction to compensate for the charge. The stored chemical energy gets converted to electrical energy in the external circuit. Interestingly, this reaction is reversible by applying an external electric current, the battery may be replenished by converting electrical energy into chemical energy. Figure 4 gives a schematic illustration of this working principle. The battery's energy storage capacity can be computed by the product of its discharge power (in watts) and discharge time (in hours). But as the battery is being cycled, over a period of time, its energy capacity is lost. This reduction in capacity depends on the charging/discharging rate as well as the temperature of operation. The voltage response of a Li-ion cell is not just defined by the electrochemical potential difference between the electrodes but also affected by reaction kinetics as well as internal cell resistance. With increasing aging of the cell, the internal impedance rises, causing higher levels of voltage under charging and lower voltage levels under discharging. This results in lower power delivery and efficiency of energy conversion. Thus, the total lifetime of a Li-ion battery is most influenced by the rise in the internal resistance (impedance rise) and progressive capacity loss (capacity fade) [8].

2

ELECTROLYTES

2.1 TYPES OF ELECTROLYTES

1. Solid-State Electrolytes (SSEs)

Solid electrolytes are materials that conduct ions but are not liquid or gel-like in nature. They can be composed of ceramic, polymeric, or composite materials. Because of their simplicity in integration and stability, SSEs have been extensively researched as a potential application in numerous electronic devices, such as portable, flexible, wearable, micro, and printable devices. Among these, polymer-based SSEs like PEO, PMMA, PVDF, and PAN are extensively researched and classified as solid polymer electrolytes (SPEs) or poly electrolytes. In comparison, fewer studies have been done on inorganic ceramic-based SSEs and hybrid organic-inorganic composites. In SPEs, the polymer matrix provides the medium for ion transport by dissolving an electrolyte salt. Experimental findings indicate that ionic conductivity is enhanced in amorphous (non-crystalline) polymer architecture. In the case of poly electrolytes, ionic transport takes place along charged polymer chains, for example, those comprising poly (acrylic acid) (PAA). SPEs simultaneously act as ion-conducting media and separators of electrodes. They also possess superb mechanical strength. Solid-state electrolytes are less prone to leakage and thermal instability than their liquid counterparts and provide higher energy density. SSEs can function effectively within a broad range of temperatures. Despite this, SSEs remain challenging, including: Low ionic conductivity Inadequate interfacial compatibility with electrodes Brittleness and cracking, which can decrease the stability of the device over long terms [9].

2. Liquid-State Electrolytes (LSEs)

Liquid electrolytes are systems in which ionic salts are dissolved in organic or inorganic solvents or in aqueous alkaline or acidic solutions. LSEs provide the highest ionic conductivity, which depends on ion size and concentration. Due to this high ionic conductivity and favorable interface interaction with electrodes, LSEs have gained popularity. In the period between 1990 and 2014, aqueous electrolytes produced using acids, bases, or salts were researched extensively because

they are low in cost, non-flammable, have low volatility, and high solubility. To circumvent the aqueous system's limitations low voltage range and narrow working temperatures several organic solvent-based electrolytes were created with solvents such as EC, DMC, EMC, DMF, and DMSO. These yield a broader electrochemical stability window (ESW). Organic LSEs, however, have limitations: High volatility and flammability Toxicity, Low ionic salt solubility, Leakage risk, making packaging harder and limiting application in wearable and portable electronics.[10]

3. Gel-State Electrolytes (GSEs)

Gel electrolytes are hybrid systems possessing characteristics of both solid and liquid electrolytes. They are formed by adding a gelling agent to a liquid electrolyte for immobilization. GSEs alleviate most drawbacks of SSEs and LSEs, such as: Low ionic conductivity Weak electrode–electrolyte contact Volatility and flammability Narrow operating temperature and voltage ranges GSEs are generally hydrogel, ionic liquid (IL), and polymeric matrix based. Ionic conductance in GSEs is realized by the polymer network hosting the ionic species. Liquid electrolytes like H_2SO_4 or ionic salts dissolved in compatible solvents are common systems used. Polyvinyl alcohol (PVA) is one of the most efficient polymers for gel electrolytes. Due to the availability of a liquid phase, GSEs provide: Higher ionic conductivity than SSEs Broad electrochemical and thermal operating windows Utilization of water as a solvent, facilitating ion conduction GSEs are eminently qualified to enable next-generation flexible, stretchable, wearable, printable, and miniaturized electronics. However, they have their challenges, including: High viscosity Sophisticated fabrication processes Limited lifespan and durability [11].

ELECTROLYTE FOR SOLID-STATE LITHIUM-ION BATTERY

Solid-state lithium-ion batteries (SSLIBs) are emerging as a transformative technology in the field of energy storage, offering notable advantages in energy density, safety, and environmental impact. This review focuses on solid-state electrolytes (SSEs) a key enabler in overcoming the limitations of traditional lithium-ion batteries (LIBs) that use liquid electrolytes. Conventional LIBs are hindered by issues such as flammability, leakage, thermal instability, narrow electrochemical stability windows, and environmental drawbacks. In contrast, SSLIBs address these concerns by incorporating solid electrolytes, which provide enhanced ionic conductivity, greater electrochemical stability, and improved safety profiles. The review examines various

classes of solid electrolytes such as oxides, sulfides, perovskites, anti-perovskites, NASICON-type, and LISICON-type materials each offering distinct structural and electrochemical advantages that promote lithium-ion transport and boost battery performance. Furthermore, it discusses recent progress in interfacial engineering, electrode material optimization, and advanced fabrication techniques. The growing potential of SSLIBs across diverse sectors from electric mobility to grid-scale energy storage is emphasized, showcasing a promising route toward safer, more efficient, and environmentally sustainable battery technologies [12].

2.2 LITHIUM ALUMINOSILICATE (LiAlSiO_4) A SOLID ELECTROLYTE

Si, Al based oxide LiAlSiO_4 (LASO) is another alternative to be used as SEs due to abundance of element have Si and Al in earth and cost effectiveness [13,14]. According to the literature, LiAlSiO_4 crystal structure has bridging of Oxygen as, SiO_4 and AlO_4 tetrahedral, and Li-ions occupying interstitial positions. LASO shows reasonable ionic conductivity as reported in earlier investigations in LASO, Li + conduction occurs along the c-axis (specifically along the 1-D channel in this direction) [15]. In recent past, the LiAlSiO_4 solid electrolyte has been prepared using numerous methods including sol-gel, magnetron sputtering, and atomic layer deposition (ALD). Since, the solid-state method is more cost-effective and scalable than other approaches, we used it to prepare the LiAlSiO_4 based SEs in the present study. Here, the sintering temperature of LASO material has been increased for better crystallinity. The impact of varying sintering temperatures on the creation of hexagonal structures during the sintering process was examined. The LASO SEs major benefits are its elemental selection and low sintering temperature (less than equal to 1000°C).

2.4 OBJECTIVES OF RESEARCH WORK

The main goal of this research is to synthesize and characterize the structural, morphological, electrical, and dielectric characteristics of the solid electrolyte LASO.

3

SYNTHESIS AND CHARACTERIZATION

3.1 SOLID STATE REACTION

This method uses solid reactants for producing polycrystalline materials. Typically, reaction begins at a very high temperature. Chemical and morphological features of reactants, including free energy, surface area, and reactivity, changes with solid-state route, and also with other reaction circumstances like reaction environment, temperature, and pressure, all have an impact on solid-state reactions. The advantages of the solid-state reaction process are its simplicity and bulk manufacturing.

Solid-state reactions are sluggish due to the inhomogeneity of the reactants at the atomic level, even if they are well mixed at the particle level (1 μm or 10 mm scale). To generate the proper ratio of desired element atomic-level mixing of reactants is done by solid-state counter diffusion of ions to bring atoms together of the various elements [16].

3.2 MATERIAL SYNTHESIS

LASO was synthesized by a typical ball-milling/ solid-state route process using high-purity precursors (Li_2CO_3 , Al_2O_3 , and SiO_2 , each with >99%). A schematic of synthesis procedure is presented in Figure 1. The precursor powders were grinding in a mortar and pestle by hand for 8 hours to create a homogeneous powder mixture. This powder was pre-sintered in a muffle furnace for 12 hours at temperatures range from 900 °C to 1050 °C. The powder thus obtained was pelletized using a hydraulic press into pellets (diameter=13mm and thickness=1.5mm). Pellets were then sintered at 1050 °C for 6 hours in a furnace to densify.

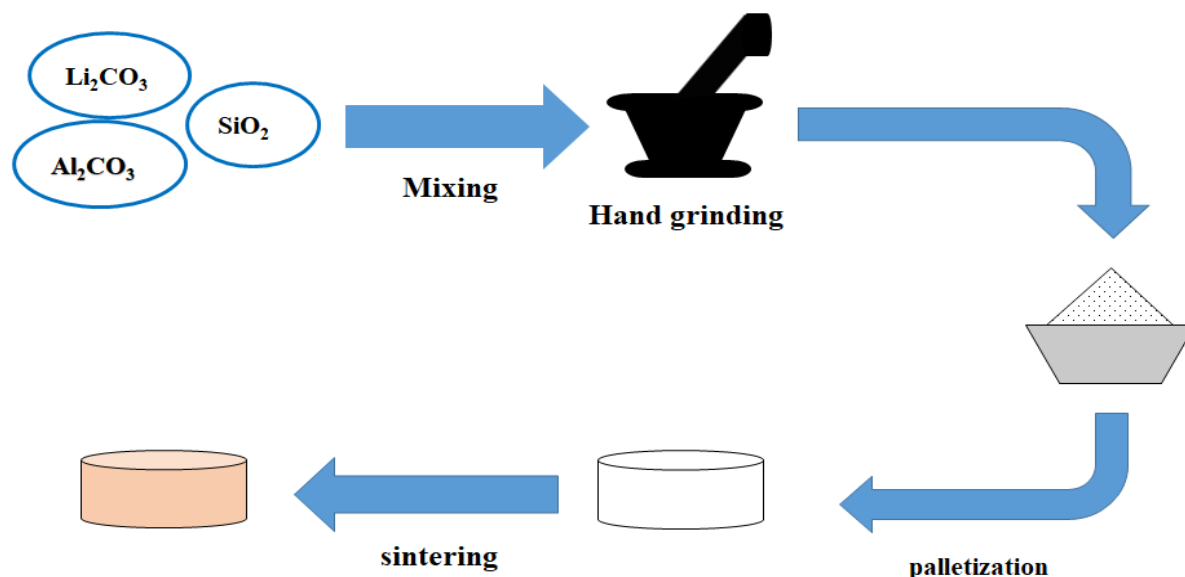


Figure 3.1- Schematic diagram illustrating the synthesis procedure of LASO via the solid-state reaction route.

3.3 MATERIAL CHARACTERIZATION

The pre-sintered (raw) LASO sample was analyzed for thermal stability and mass loss using a Perkin Elmer TGA 4000 thermogravimetric analyzer (TGA) along with differential scanning calorimetry (DSC). For phase identification, the synthesized sample was examined using X-ray diffraction (XRD) with a Bruker D-8 diffractometer, employing a $\text{CuK}\alpha 1$ radiation source ($\lambda = 1.54 \text{ \AA}$) over a $10\text{--}80^\circ$ range with a step size of 0.02° . The microstructure of the sintered pellet was examined with a Scanning Electron Microscope (SEM), in this case the FEI Nova NanoSEM at 15 kV. The electrical properties and frequency response of the LASO pellets were characterized using a HIOKI 3532 LCR meter over the frequency range of 1 MHz to 4 Hz, from 90°C to 140°C temperatures. To allow electrical conductivity for measurement, silver electrodes were applied to both sides of the sintered pellets by utilizing a HindHi-manufactured thermal evaporation unit.

3.4 XRD

Crystal materials can be recognized and described using X-ray diffraction (XRD), a conventional technique. An X-ray pattern unique to each crystalline solid serves as a "fingerprint" for identification. The approach is based on the sample's X-ray diffraction in multiple directions. There is significant diffractive interference with waves at wavelengths close to the crystal lattice spacing. With a wavelength of 1.54 \AA , copper is utilized as source of X-ray. The measurement of diffracted X-ray intensity is based on the diffraction angle (2θ). The atomic structure can be inferred from the peak's intensity. The crystal's perfection is reflected in the peak's sharpness and form.

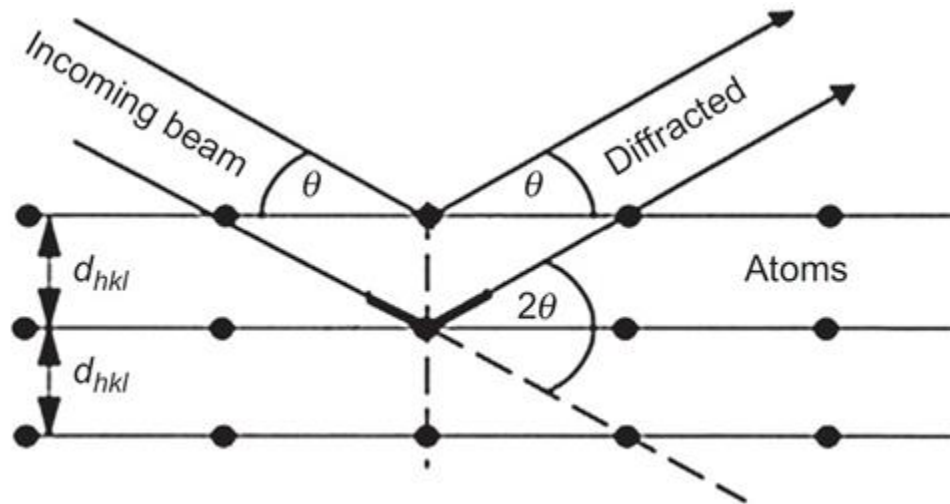


Figure 3.2: Geometric conditions for diffraction from lattice planes.

The intensity Vs. 2θ plot-

- (i) Provides structural information about the material. The presence or absence of specific sets of peaks corresponding to distinct planes determines the crystal formations.
- (ii) The movement of peaks from their initial locations in bulk crystals indicates stresses in the material.

W.L. Bragg provided a geometrical description of the XRD phenomena, known as constructive interferences. The figure 3.3 illustrates geometrical conditions of diffraction and deduction of Bragg's law. Bragg's law is provided as an Equation (3.1).

$$2d\sin\theta = n\lambda \quad (3.1)$$

In Equation (3.1), n represent order of diffraction, θ is angle of diffracted beam, λ is x ray wavelength and d is the interplanar spacing. Diffraction follows Bragg's equation for constructive interference when it happens along each lattice plane and direction in a polycrystalline, untextured material containing small grains.

For qualitative analysis, X-ray diffraction is primarily used, despite being a quantitative process. Any crystalline solid, including organic materials, metals, insulators, polymers, ceramics, and thin film powders, is subject to this kind of analysis. For both single crystals and powders, X-ray diffractometers can be employed. While single crystal diffractometers are used to research molecular structure, powder diffractometers are used to analyze phases, however the latter may also be used to extract molecular information [17].

3.5 SEM

Scanning Electron Microscopy (SEM) is well known and utilized in various scientific disciplines for high-resolution imaging of organic and inorganic materials at the nanometer to micrometer length scale. Current SEM equipment is capable of reaching magnifications of as much as 300,000x and in certain cutting-edge models even 1,000,000x. SEM produces very high-detail grayscale images of the surface of samples and is thus precious in materials characterization.

Additionally, SEM can be used in conjunction with Energy Dispersive X-ray Spectroscopy (EDS) to provide qualitative and semi-quantitative elemental analysis. These ancillary methods allow for a thorough composition appreciation of the sample, exceeding the reach of standard laboratory techniques. SEM is based on electron emission.

Scanning Electron Microscopy (SEM) provides a window on the otherwise hidden domains of micro- and nanoscale structures. It allows researchers to see detailed information that lies beyond the resolution capabilities of optical microscopy. As described by Goldstein et al. [5], and further explained in next figure section, SEM functions via a clear cut series of processes:

- a) **Electron Beam Generation:** The SEM makes use of a concentrated beam of high-energy electrons with an energy range of between 100 and 30,000 electron volts (eV). The electrons are generally produced from a thermionic source.
- b) **Beam Focusing and Interaction:** The primary electron spot produced by the gun is too wide for high-resolution imaging. Thus, SEM incorporates electromagnetic lenses that constrict and concentrate the beam on to the specimen. Final spot size of the beam is usually smaller than 10 nanometers (nm). When this concentrated beam hits the sample surface, it goes as deep as approximately 1 micrometer (μm), producing different signals that are utilized to form the image.
- c) **Raster Scanning Mechanism:** SEM forms the image by scanning the electron beam across the specimen in a raster fashion point by point, line by line. This is regulated by scanning coils, which direct the beam across the sample. To produce higher magnification, the coils decrease the area to be scanned, zooming in on smaller regions of the surface. Working distance — the distance between the last lens and the surface of the specimen, also affects magnification but is usually automatically regulated in modern SEM systems.
- d) **Signal Detection:** When the electron beam is interacting with the sample, it produces signals in the form of secondary electrons (SE) and backscattered electrons (BSE). The detector gathers these electrons to create the final image. In the absence of a detector, the emitted signals would create a disordered and unreadable image. By using a positive voltage on the detector's collector screen, both SE and BSE are detected; a negative voltage leads to detection of only BSE. A scintillator detector (as indicated in Figure 9) is widely utilized for the detection of both SE and BSE.
- e) **Image Display and Adjustment:** The obtained signals are displayed on a screen. The operator may set parameters like brightness and contrast to make the image clearer. For finer structural details to be viewed, magnification levels higher than 10,000x might be necessary.
- f) **Accelerating Voltage Effect:** The energy of the electron beam influences the character of the information that is obtained. Low accelerating voltages (less than 5 kV) yield detailed surface information, while high voltages (15–30 kV) enable electrons to penetrate and access information below the surface. Figure 3.2 shows the differential electron penetration depths and resulting signals.

g) 3D Surface Topography: SEM is also capable of pseudo three-dimensional imaging by recording surface shape, size, and texture variations. The topographical contrast is heavily dependent on the amount of SE and BSE signals detected. Surprisingly, by tilting the sample surface between 50° and 70° , the number of emitted electrons is enhanced, and thus topographic contrast and depth vision are greatly improved[18].

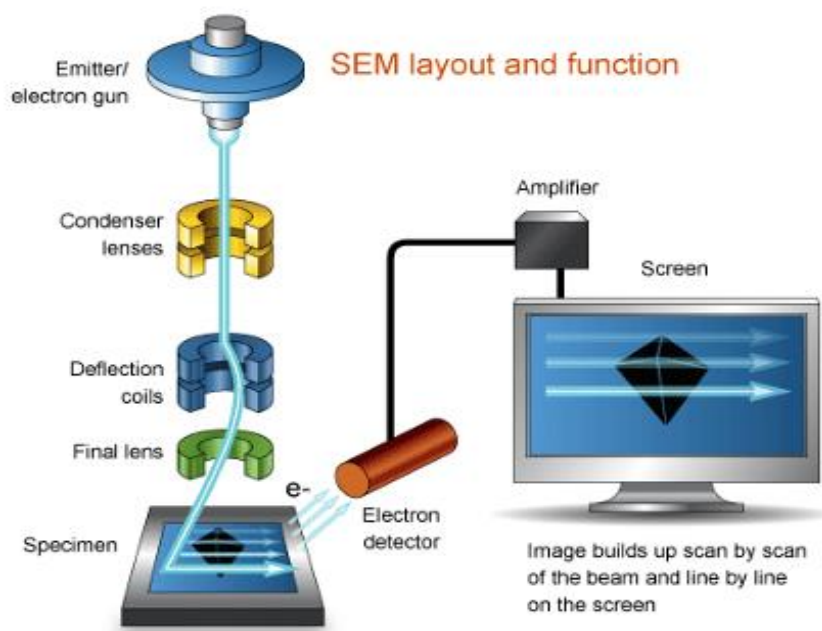


Figure 3.2 Schematic diagram of the SEM setup illustrating major components

3.6 TGA

Thermogravimetric Analysis (TGA) is a thermal analysis that measures the absolute weight and weight change rate of a material with respect to time or temperature in a controlled atmosphere. TGA gives useful information about different properties of materials, including thermal and oxidative stability, responses in different gaseous environments, moisture and volatile contents, and, in certain cases, the composition of multi-component systems. It also helps to decide how components of a sample are alternatively held together, based on their individual thermal responses. When Differential Thermal Analysis (DTA) or Differential Scanning Calorimetry (DSC) is used along with TGA, the technique becomes Simultaneous DSC-TGA (or SDT). SDT

allows the benefits of TGA (measurement of weight loss) to be coupled with the detection of heat flow of DSC. This enables the examination of not just mass change but also of thermal transitions, including melting, boiling points, and heats of reaction.

TGA basically measures three important parameters: Sample weight, Rate of change in weight, i.e., Differential Thermogravimetry (DTG), Temperature

The DTG curve is obtained as the first derivative of the weight with respect to time or temperature. This curve is very convenient for qualitative and quantitative analysis. Qualitatively, it is used to identify materials and separate overlapping reactions. Quantitatively, it gives information like peak height and the temperature of maximum weight loss. In a TGA experiment, the test sample is subjected to a controlled heating rate in a definite atmosphere (e.g., air, nitrogen, carbon dioxide, helium, or argon). Temperature increases progressively, and the sample weight is constantly monitored as a function of temperature or time. The obtained plot of weight change vs temperature is referred to as a thermogravimetric curve or thermogram.

Mechanisms of Weight Change in TGA

Weight Loss can be caused by:

- a. Decomposition – chemical bond breaking
- b. Evaporation – loss of volatile components on heating
- c. Reduction – reaction with a reducing environment (e.g., hydrogen, ammonia)
- d. Desorption – departure of adsorbed species from the sample surface

Weight Gain can be caused by:

- a. Oxidation – reaction with an oxidizing environment
- b. Adsorption or Absorption – adsorption or absorption of gases in the surrounding environment

DSC

Differential Scanning Calorimetry (DSC) is a major thermal analysis technique, since heat flow changes accompany all phase transitions. Endothermic transitions, including melting, need energy (absorbed heat), while exothermic transitions, such as crystallization, emit energy. The energy is usually quantified in Joules per gram (J/g).

DSC has a number of advantages:

- a. It needs only minute quantities of the material (1–10 mg)
- b. Compatible with analyzing solids and liquids
- c. Rapid analysis times, typically between 10 and 30 minutes
- d. Easy sample preparation
- e. The majority of current DSC equipment features automated sampling and data analysis functionality

3.7 Impedance analysis

Impedance spectroscopy (IS) represents a technique for analysing frequency-dependent electrical characteristics such as impedance, admittance, conductance, and dielectric properties in ceramic and bulk materials. This analytical approach helps distinguish different electrical polarization mechanisms by examining their characteristic time constants and relaxation frequencies. The methodology finds applications across various material types including dielectric substances, ionic compounds, and electronic conductors.

Common applications include energy storage and conversion systems such as supercapacitors, electrochemical cells, and fuel cells, along with electroceramics, solid electrolytes, and dielectric materials including polymers and glasses. Within electrochemistry, this technique serves as a fundamental tool for examining electrode kinetics and is commonly referred to as electrochemical impedance spectroscopy (EIS).

The fundamental principle involves applying sinusoidal perturbations (alternating voltage or current) across a broad frequency spectrum (typically Ω to MHz) to disturb electrical or

electrochemical systems at equilibrium or steady-state conditions. The system's sinusoidal response (current or voltage output) to these external perturbations is then measured and analyzed.

Systems studied through electroceramics or electrochemistry are characterized as linear time-invariant systems, meaning their response remains consistent across time within the tested frequency range. The output signal (alternating current or voltage) maintains a controlled, linear relationship with the input signal (alternating voltage or current) via the "transfer function" methodology of IS.

Through IS implementation, researchers can identify and often separate reactions occurring within bulk materials or devices, detect internal and external interface presence, and gather data regarding charge storage and energy dissipation mechanisms. Modern instrumentation readily enables frequency measurements spanning 1 to 12 orders of magnitude.

This methodology has proven valuable for characterizing traditional capacitors, fuel cells, batteries, and photovoltaic cells due to their diverse electrical behaviors and multi-material properties. IS has also been employed for monitoring component aging in both structural and electrical systems and for quality assessment of solid-state capacitors. The technique extends beyond energy-related applications to any material or device requiring characterization of component contributions from grain, grain boundary, and interface interactions, along with their frequency-dependent behaviors at room temperature or various operating temperatures.

High-conductivity materials exhibit optimal representation through conductivity as a temperature and operational environment function (vacuum or pressure conditions), while dielectric-type materials are better characterized using dielectric formalism, or in some cases, both approaches. Material type and research objectives determine the selection of appropriate electrical processes, with several electrical processes potentially occurring simultaneously.

Polarization phenomena in polycrystalline materials result from reduced electrical conductivity at grain boundaries relative to grain interiors. Three potential explanations exist for this decreased conductivity: space charge accumulation at grain boundaries, grain charge variations contributing significantly to ceramic understanding in electrochemical applications like solid oxide fuel cells.

In electrochemical contexts, grain boundaries play essential roles in determining nonlinear current-voltage relationships across electrodes and temperature-dependent electrolytic behavior. Additionally, material electrical resistance decreases with rising temperature, known as negative temperature coefficient of resistance (NTCR). This characteristic contradicts typical conductive materials' behavior, where resistance increases with temperature, and temperature-dependent charge carrier mobility or concentration represents the primary factor in NTCR materials.

Impedance demonstrates inverse relationships with dielectric polarization magnitude and frequency relationships within permittivity, permeability, and attenuation measurement techniques. Readers seeking comprehensive research should consult detailed articles where information is systematically organized within thoroughly analysed impedance data, interpretable through impedance-to-other-electrical-terms conversions like admittance, conductivity, permittivity, and other electrochemical parameters.

EIS spectroscopy capabilities enable discrimination and comprehensive information provision for various electrical, electrochemical, and physical processes occurring within actual electrochemical systems, distinguishing it from other electrochemical methodologies. This technique exhibits unique temporal behavior ranging from rapid to gradual responses, with different time constants displayed through various electrochemical processes dependent on multiple factors including electrode kinetics, mass transfer phenomena, material properties, and electrode-electrolyte interface characteristics.

For solid polycrystalline electrolytes, electric double layer charging or discharging at electrode-electrolyte interfaces, impedance relationships of electric double layers based on electrode morphology and electrolyte composition, electrode charge-transfer reactions related to homogeneous reactions, and adsorption/desorption phenomena, along with diffusion-controlled mass transfer processes, represent key analytical considerations.

4

RESULTS AND DISCUSSION

4.1 THEORETICAL ANALYSIS OF LASO SEs CRYSTAL STRUCTURE

Experimental preparation of several lithium aluminosilicates is possible, and The Materials Project Database [19] has information about them, the crystal structure information for the LASO solid electrolyte is listed in Table 1, and the related structural model is shown in Figure 4.1. High-lithium-content aluminosilicates have been found to be good ionic conductors owing to their narrow bandgap and the availability of many mobile lithium ions [20].

Table 1. Crystal structure parameter of LiAlSiO_4 observed from Materials Project Database [19]

ID	mp-558713
Formula	LiAlSiO_4
Crystal system	hexagonal
Space group	P_{622}
Band gap(eV)	4.51

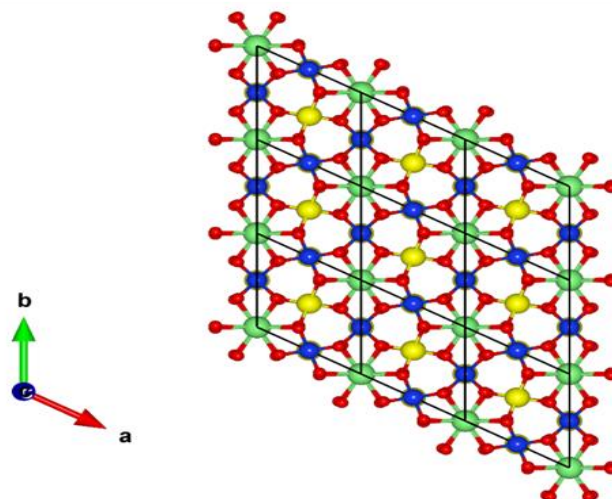


Figure 4.1 Representation of Crystal structures of LiAlSiO_4 (using VESTA), Li is green, Si is blue, Al is yellow and O is red.

4.2 TGA AND DSC ANALYSIS

Sintering of LASO ceramics by the traditional solid-state approach is challenging, mainly because of lithium volatilization in the form of Li_2O [21]. In order to determine the thermal stability and find a suitable sintering temperature, TGA combined with DSC was performed on hand-grinded powder sample between room temperature to 850 °C in air, as shown in Fig. 3. A slight mass gain was first noted between room temperature to about 100 °C and can be explained as the adsorption of atmospheric gases or moisture onto the sample surface. As the precursors like Li_2CO_3 and SiO_2 are hygroscopic and have a tendency to absorb water, leading to a small gain in mass. This process will not include much thermal action and therefore the DSC curve is flat [22]. The mass loss in the region of 100 °C to 300 °C is gradual, which is believed to relate to the loss of physically adsorbed water and volatile contaminants [23]. This procedure usually comes with an endothermic peak on the DSC signal, relating to the energy needed for desorption. A sudden mass loss of about 10.57% is subsequently observed in the range 300 °C to 600 °C, which is mainly attributed to the decomposition of Li_2CO_3 into Li_2O and CO_2 , where the latter is responsible for the weight loss. Such decomposition is generally accompanied by an endothermic phenomenon in the DSC trace [24,25]. Then, another major mass loss of approximately 11.46% occurs from 600 °C to 700 °C, this mass loss corresponds to the thermal decomposition of Li_2CO_3 to Li_2O and CO_2 gas. A sharp endothermic peak is occurring between this temperature. After the 700 °C small thermal event is found in the DSC trace that is not accompanied by a corresponding mass change. This process is the solid-state reaction between Li_2O (from the earlier decomposition), Al_2O_3 and SiO_2 to produce LiAlSiO_4 [23]. From the thermal analysis, it is deduced that the sintering temperature in LASO ceramics ought to be above 800 °C in order to secure the completion of intermediate reaction and formation of stable crystalline phases. But temperatures have to be regulated with care to limit lithium evaporation and avoid excessive grain growth. A best sintering temperature is found at ~ 900 °C, at which the favorable phase stability is attained with the least weight loss.

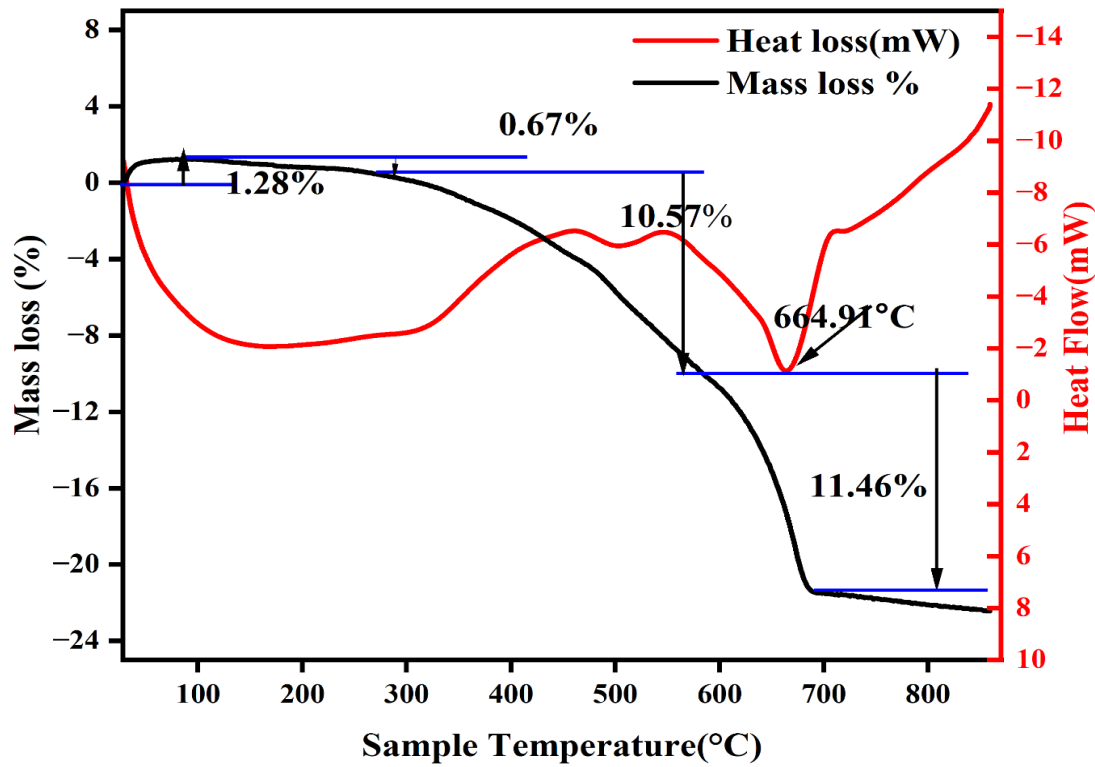
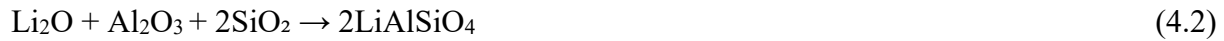


Figure 4.2 TGA/DSC curve of hand-grinded sample of LASO from room temperature to 850°C in air atmosphere



4.3 XRD ANALYSIS

An essential step in the manufacture of SE is sintering, which can change the electrolyte's structural characteristics by raising its relative density and lowering its bulk and grain boundary resistance. For this reason, selecting the right sintering environment and optimizing the sintering temperature and duration are crucial to achieving the desired structure. Optimizing the composition of the ceramic electrolyte and preventing lithium loss during sintering are also necessary [26]. TGA results shows the sintering temperature range for LASO ceramics is above 800 °C to ensure complete reaction and phase stabilization and, at the same time, minimizing lithium volatilization.

The X-ray diffraction (XRD) pattern of the LASO sintered at the different temperatures ranging from 900 °C to 1100 °C with temperature step of 50 °C for 12 hours respectively at each step is shown in figure 4.3 (a) to study the formation of the LASO structure as predicted from TGA/DSC curves discussed in previous section. The XRD analysis shows a defined crystalline LASO at 1000 °C, crystal structure under this temperature is affected by the balance between kinetic and thermodynamic stability. At the optimal sintering temperature, atomic or ionic species rearrange into the most thermodynamically favorable crystal structure through the minimization of the system's Gibbs free energy [27].

The structural characteristics of electrolyte at different sintering temperature were determined by XRD analysis. A rise in the sintering temperature is equivalent to an increasing improvement in the intensity of the LASO electrolyte's diffraction peaks, sharp peaks represent an enhancement in crystallinity and phase stabilization of the LASO crystal system [28].

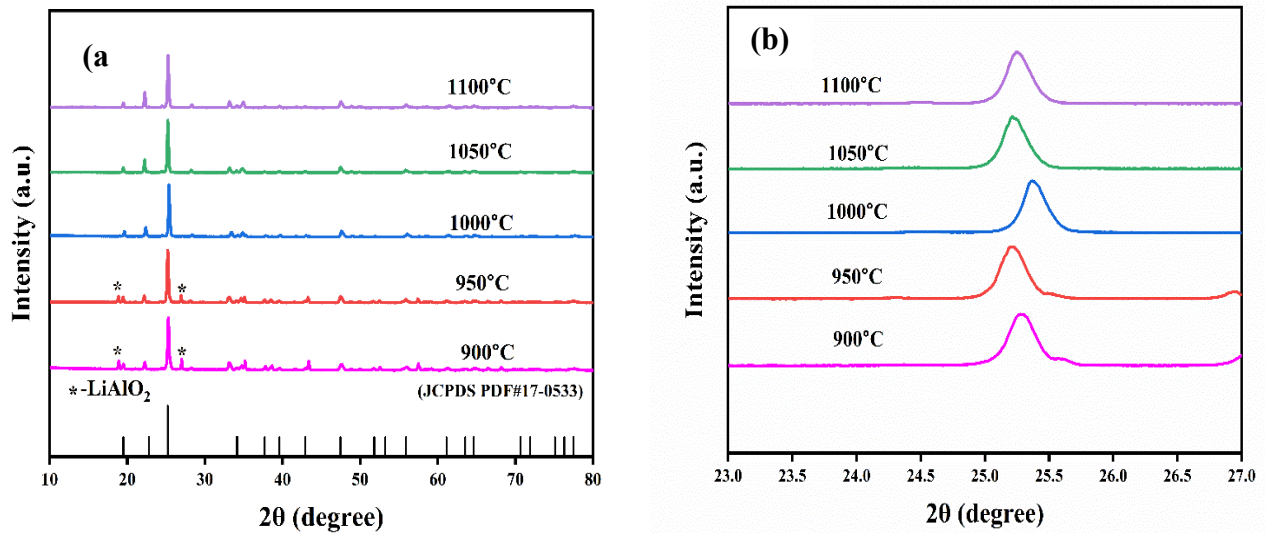


Figure 4.3 (a)XRD images of the LASO material after the material was sintered at various temperatures (b) XRD patterns of the $d_{(102)}$ plane at various sintering temperatures.

The electrolytes sintered at 900 °C and 950 °C includes some trace amounts of LiAlO_2 impurities due to unfavorable reaction of silicon and oxygen atoms during sintering, whereas the XRD patterns of the electrolytes sintered at above 950 °C crystallizes in LiAlSiO_4 phase (JCPDS PDF#17-0533)[35-37]. The creation of a lithium-depleted phase, possibly because of lithium volatilization at high temperatures, resulted in the decrease of crystallinity of the electrolyte upon

sintering of the pellets at 1050 °C or higher. Thus, 1000 °C was identified to be the optimal temperature for obtaining the pure LiAlSiO₄ phase.

Figure 4.3(b) shows, as the temperature rises, the material's crystallinity improves: Higher temperatures (particularly 1000°C) cause the peak becomes sharper and more intense, indicating improved crystal formation and reduced lattice deficiencies. The peak position (around 25.2°) varies slightly with temperature, which could be a sign of lattice strain or minor temperature-induced changes in lattice characteristics.

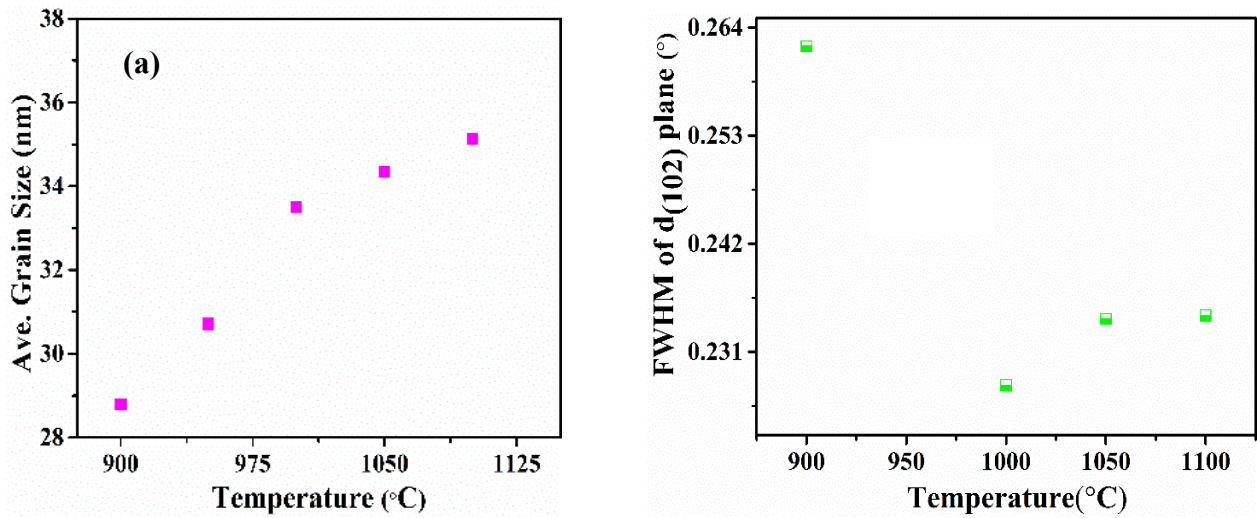


Figure 4.4 (a) A graph showing the relationship between the LASO SEs' average grain size (nm) and sintering temperature (°C). (b) Temperature versus the d₍₁₀₂₎ plane spacing plot of LASO SEs

The figure 4.4(a) plots the average grain (crystallite) size of the LASO SEs versus temperature. The average grain size of LASO was determined using the Debye-Scherrer's equation (4.3).

$$D = \frac{k\lambda}{\beta \cos(\theta)} \quad (4.3)$$

$$\beta t = \frac{k\lambda}{D \cos(\theta)} + 4\epsilon \tan(\theta) \quad (4.4)$$

Where θ represents the Bragg's scattering angle, β denotes the peak width at half-maximum intensity (FWHM), the X-ray wavelength $\lambda = 0.15418$ nm, and the Scherrer's constant $K=0.9$. One crucial factor affecting the crystallite dimensions of the LASO-based solid electrolytes is the processing temperature. LASO 900°C, LASO 950°C, LASO 1000°C, LASO 1050°C, and LASO 1100°C exhibit mean crystallite dimensions of 28.78, 30.71, 33.5, 34.35, and 35.12 nm respectively. The mean crystallite dimensions expanded with increasing processing temperature. Grain boundaries migrate when the sintering temperature rises, and the sintering temperature has a significant impact on grain growth.

Higher crystallinity in ceramic solid electrolytes is necessary to enable effective lithium-ion transport. From XRD patterns, the FWHM of the (102) major peak decreased to enhance the crystallinity of electrolytes. The FWHM and sintering temperature relationship are shown in the figure 4.4 (b). The FWHM of the XRD peak has an inverse relationship with the crystallinity. At the processing temperature of 950°C, the (102) scattering peak exhibited notable widening and elevated full width at half-maximum intensity (FWHM) of 0.25°, indicating poor crystallinity. At 1000°C, the crystallinity became saturated and significantly enhanced. At this point, maximum crystallinity was achieved and the LASO displayed a sharp and distinct peak with the narrowest FWHM (0.22°). However, the elevated resistance observed in the specimen processed at 1050°C is caused by lithium volatilization at high temperature leading to the formation of a lithium-deficient phases. Thus, the superior ionic conductivity of the pellet processed at 1000°C with no LiAlO₂ impurities (as shown by the XRD results) was proved. As a result, 1000°C was determined to be the ideal sintering temperature for creating LiAlSiO₄ based SEs.

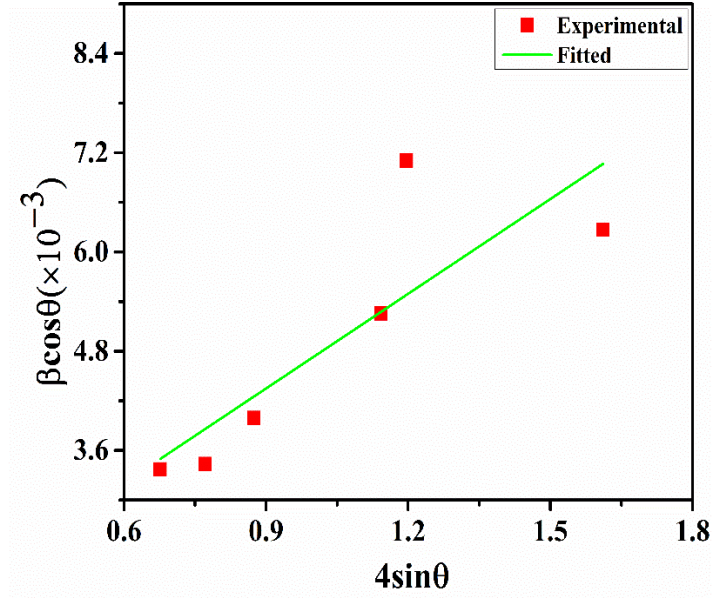


Figure 4.5 W-H plot of LASO sample

The Williamson-Hall plot, which is used to calculate the micro-strain from the total peak broadening of diffraction peaks using the expression given in Equation (4.4) is displayed in Figure.6. In this case, the symbols β_t , β , λ , ε , D , and K stand for total peak broadening, full width at half maximum, X-ray source wavelength (1.54 Å), micro-strain, crystallite size, and form factor (0.9), respectively. For the purpose of calculating crystallite size, the peaks have been used to compute the average full width at half maxima. The slope of the fitted plot between $4\sin\theta$ and $\beta\cos(\theta)$ indicates the micro-strain achieved in the system. The average crystallite size estimated from Scherrer's equation is 32.49 nm and the micro-strain in the crystal lattice, obtained from Williamson-Hall (W-H) analysis, is found to be 2.58×10^{-3} [32]. This analysis indicates the sub-micron crystallite size range, which contributes to improved sintering and a reduction in the bare material's sintering temperature.

4.4 MORPHOLOGICAL RESULTS

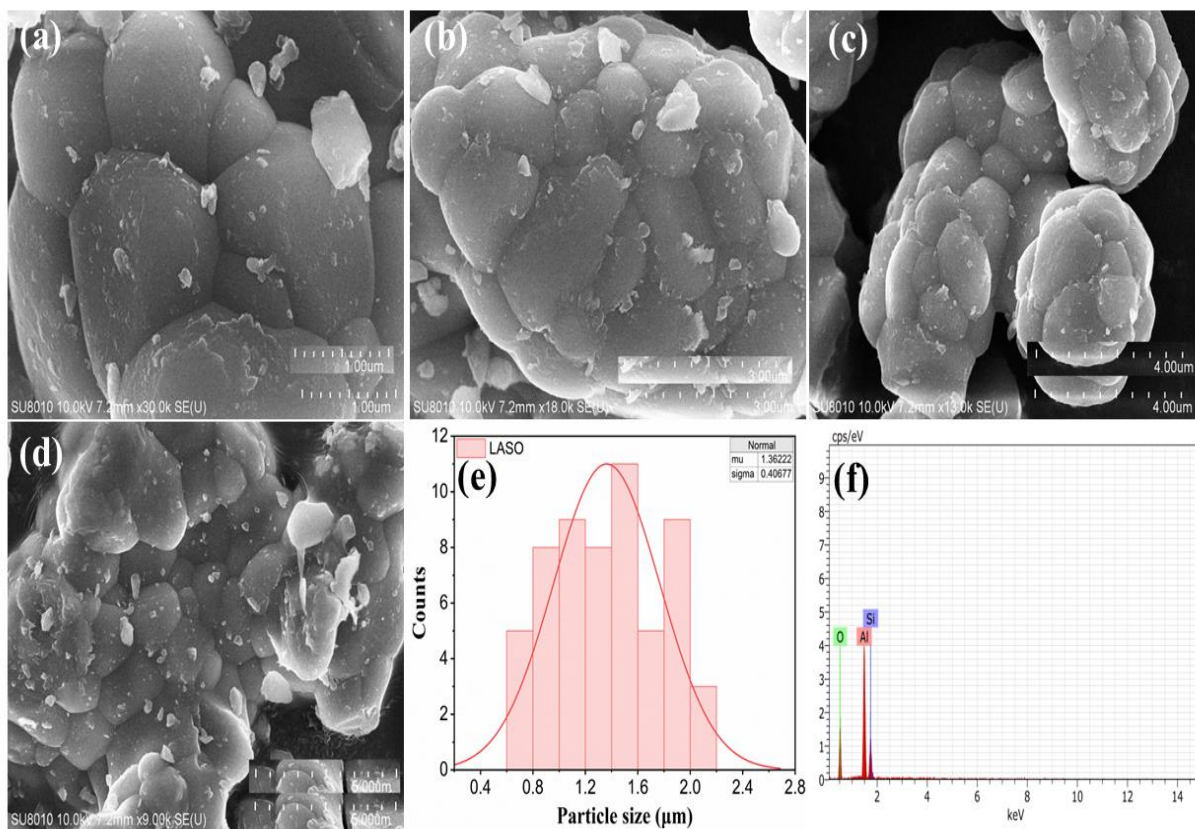


Figure 4.6(a, b, c, d) SEM images of the LiAlSiO₄ material prepared using the solid-state method (and sintered at 900 °C) at different magnifications, and (e) Particle size distribution graph for the LASO particles, (f) EDX of the LiAlSiO₄ material

Fig.4.6. (a,b,c,d) shows SEM results of LiAlSiO₄ pellets sintered at various microscopies in the range of 1.00 μm-5.00 μm at 1000 °C. In XRD analysis section, at 1000 °C material have the maximum crystallinity. Fig. 4.6(e) shows the particle size distribution of the SEM images in the range of 1.00 μm-5.00 μm, here the average particle size calculated is 1.36 μm. Figure 4.6(f) shows the EDX of the LiAlSiO₄ sample which suggests that the composition of this sample shows a higher proportion of oxygen and aluminium and a lower proportion of silicon. Table 2 displays the element proportion in structure of the sample.

Table 2. Elemental Identification of LiAlSiO₄

Element	Norm. C (wt.%)	Atom. C (%)	Error (wt.%)
Aluminium (Al)	~41%	~32%	±4.0
Oxygen (O)	~41%	~54.7%	±15.0
Silicon (Si)	~17%	~13%	±1.8

4.5 DIELECTRIC ANALYSIS

The dielectric response signifies the material's capacity to store electrical energy, the subsequent relaxation processes and its frequency response at different temperatures[33].

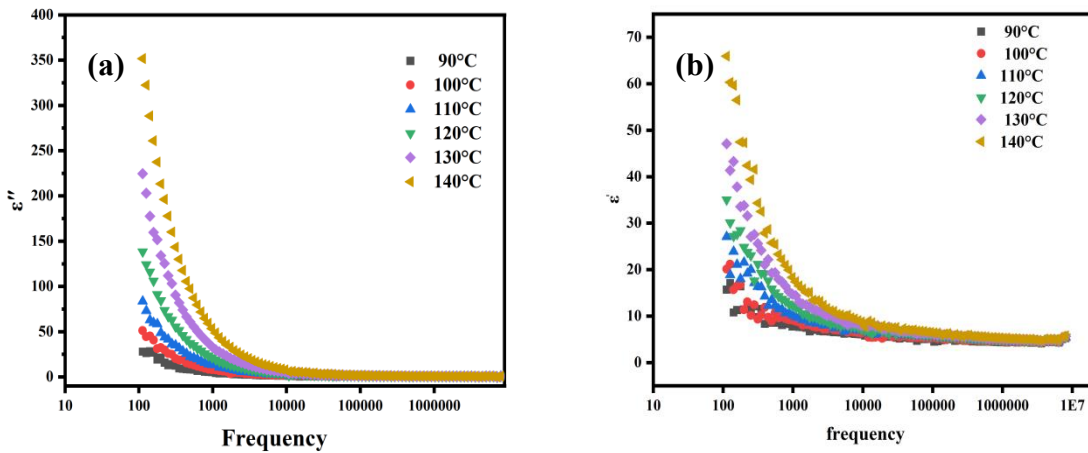


Figure 4.7 (a) The curve between real part of permittivity vs frequency of the sample LASO
(b) The curve between imaginary part of permittivity vs frequency of the sample LASO

This analysis provides information regarding two important material properties: (a) dielectric permittivity and (b) dielectric dissipation. When alternating current fields are imposed, thermal energy is produced through charge carriers resulting from delayed polarization responses, commonly termed dielectric dissipation. The overall dielectric permittivity of a substance is influenced by temperature, pressure, frequency response, and molecular structure parameters. The relative permittivity (commonly referred to as total dielectric permittivity) comprises the actual

(ϵ') and theoretical (ϵ'') components combined with the dielectric dissipation factor (D) which is determined through fundamental equations referenced in earlier studies.

Figure 4.7 (a, b) demonstrates how ϵ'' and ϵ' vary with frequency across different temperatures. At reduced frequencies, a domain of elevated dispersion with increased permittivity values corresponds to the existence of the Maxwell-Wagner relaxation mechanism and interfacial polarization as documented in similar ceramic solid-state electrolyte studies. The elevated permittivity values at reduced frequencies can be attributed to numerous well-conducting grains with reduced grain boundary conductivity.

Charge carriers can readily traverse across the grains and accumulate at grain boundaries when an external electric field is applied. With increasing temperature, charge carriers in dielectric substances gain sufficient energy to move more efficiently along the direction of the imposed electric field. This transport results in charges accumulating on the higher energy barrier region, originating from the reduced energy region, thereby enhancing charge accumulation, which subsequently increases polarization and permittivity responses [34].

4.6 IMPEDANCE ANALYSIS

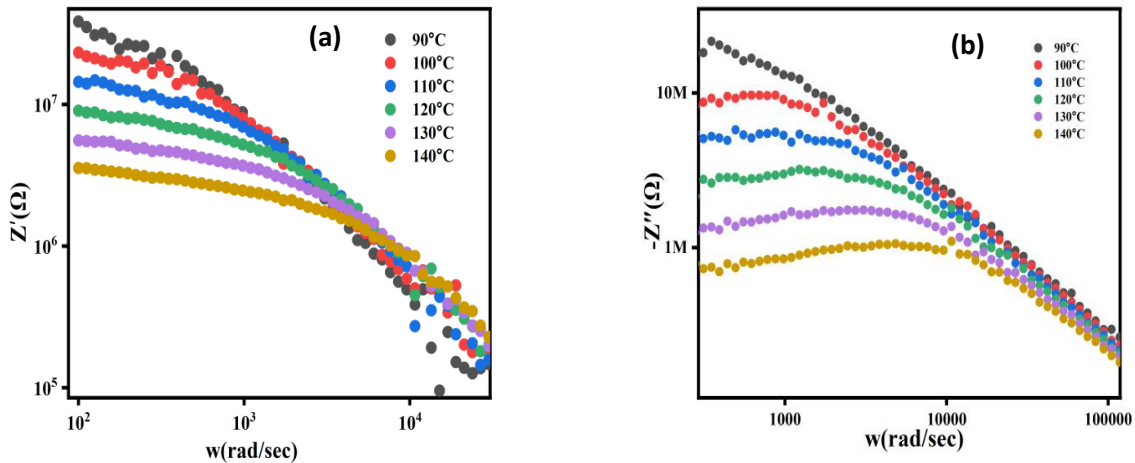


Figure 4.8 (a) The curve between real part of impedance vs frequency of the sample LASO (b) The curve between imaginary part of impedance vs frequency of the sample LASO

Complex Impedance Spectroscopy (CIS) is an effective technique utilized to study the relaxation behavior of various microscopic areas in ceramics [35]. Figure 4.8 (a, b) shows the frequency variation of the real (Z') and imaginary (Z'') components of impedance at different temperatures of 90 to 140°C. Figure 9(a) illustrates that Z' is decreasing with rising temperature and frequency, which signifies a negative temperature coefficient of resistance (NTCR) and is indicative of increased conductivity of the material [36].

However, at high frequencies ($\geq 10^4$ rad/sec), the trend changes, the real part of impedance for 140°C becomes higher than that for 90°C and the curves do not merge. This anomalous behavior suggests that at higher frequencies the electrical response is no longer dominated by simple conduction. Instead, interfacial phenomena, such as grain boundary polarization (Maxwell-Wagner effect), and the frequency dependent dielectric properties of the material become more significant [48,49]. Figure 4.8 (b) shows, as the temperature rises value of Z'' decreases in lower frequency region due to enhanced ion mobility, reducing polarization losses and flattening any low frequency peaks, which implies faster charge transfer at interfaces. In the intermediate frequency range (10^3 – 10^4 rad/s), a peak in Z'' emerges, corresponding to grain boundary or bulk relaxation, with the peak frequency (f_{\max}) providing the relaxation time ($\tau = 1/2\pi f_{\max}$). With increasing temperature, this peak shifts to higher frequencies, reflecting shorter relaxation times due to thermally activated dipolar or ionic reorientation. Figure 4.9 demonstrates the Nyquist plots of Z' versus Z'' for LASO ceramics at different temperatures. The Nyquist plot show depressed semicircular arc, each representing the impedance response at a specific temperature. These depressed semicircular arcs indicated the deviation from ideal dielectric behavior of the material. This depression occurs because the system exhibits a distribution of relaxation times rather than a single relaxation time, suggesting microscopic inhomogeneity in the material's structure or composition. The arcs shift systematically toward the origin (lower impedance values) as temperature increases from 90 °C to 140 °C, demonstrating that both the resistive and reactive components of impedance decrease with rising temperature. This behavior clearly shows the thermally activated nature of charge transport in LASO, where increased thermal energy enhances ion mobility. The diameter of these depressed arcs, which corresponds to the material's resistance, becomes smaller at higher temperatures, corresponds to the NTCR behavior and indicates improvement in conductivity of material. The elevated-frequency intercept on the real axis (Z')

indicates bulk resistance, while the lower frequency domain displays the onset of a secondary arc or tail, indicating supplementary interfacial or diffusive mechanisms at reduced frequencies. These phenomena can be represented through an equivalent circuit comprising parallel arrangements of resistance and constant phase elements (CPE) rather than perfect capacitors to explain the non-ideal characteristics observed in the compressed semicircles.

Overall impedance is modeled using equivalent circuit (R1-(R2-CPE2)||CPE1)) as demonstrated in the figure 4.9 (a) inset using EIS analyzer software. Here R1, R2 represent electrode resistance, bulk resistance and CPE1, CPE2 represent constant phase elements. The theoretical (Z'') and actual (Z') components of the complex impedance are described by the subsequent equations [34].

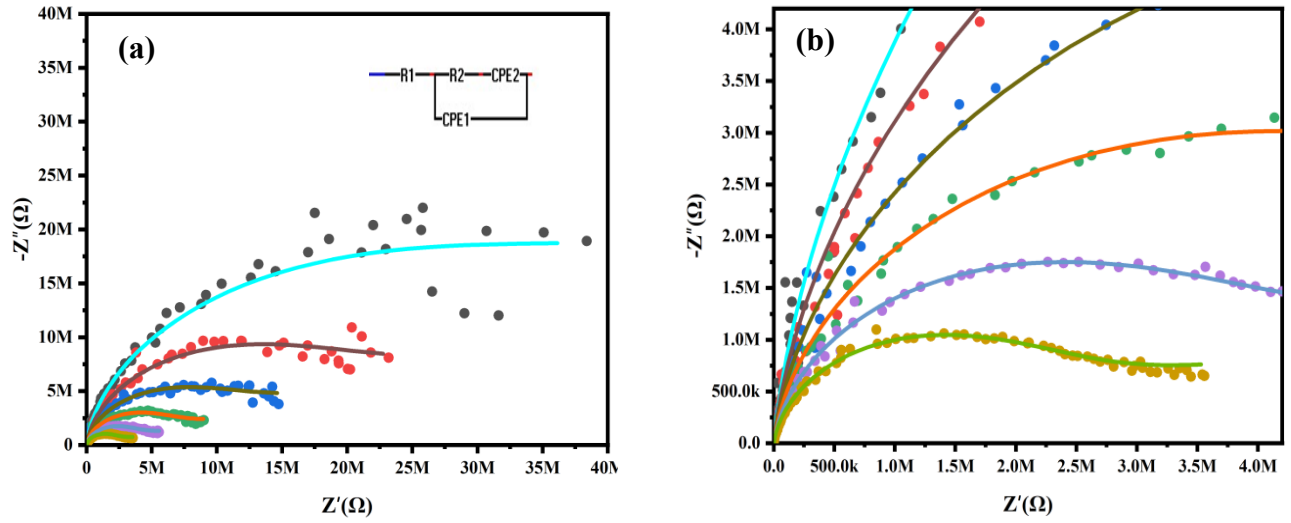


Figure 4.9 (a) Nyquist representation of LASO specimen across thermal conditions from 90°C to 140°C (b) Nyquist representation of LASO specimen with magnified view, thermal conditions from 90°C to 140°C

$$Z' = \frac{R1}{[1+(\omega R1C1)^2]} + \frac{R2}{[1+(\omega R2C2)^2]} \quad (4.5)$$

$$Z'' = \frac{\omega R1^2 C1}{[1+(\omega R1C1)^2]} + \frac{\omega R2^2 C2}{[1+(\omega R2C2)^2]} \quad (4.6)$$

R_1 and C_1 represent the resistive and capacitive characteristics of the grain core regions, while R_2 and C_2 represent the grain interface resistive and capacitive properties; ω denotes the angular frequency. The ionic conductivity of the consolidated pellets is determined using Eq (4.7):

$$\sigma = \frac{L}{R \times A} \quad (4.7)$$

Where R indicates the resistance of the analyzed sample in Ω , A represents area in cm^2 and L denotes the thickness of the pellet in cm, respectively. The bulk ionic conductivity (σ) of the LASO material is observed as $1.94 \times 10^{-5} \text{Scm}^{-1}$ at 140°C . Figure 3 demonstrates the thermal dependency of the conductivity calculated using Arrhenius Equation expressed by Eq (4.8):

$$\sigma = \sigma_0 e^{\frac{-E_a}{KT}} \quad (4.8)$$

Where σ indicates the ionic conductivity, σ_0 denotes the pre-exponential factor, E_a represents the activation energy, K indicates the Boltzmann constant and T denotes the absolute temperature. The activation energy graph provides understanding of the energy barrier for a process and the thermal dependence of reaction dynamics.

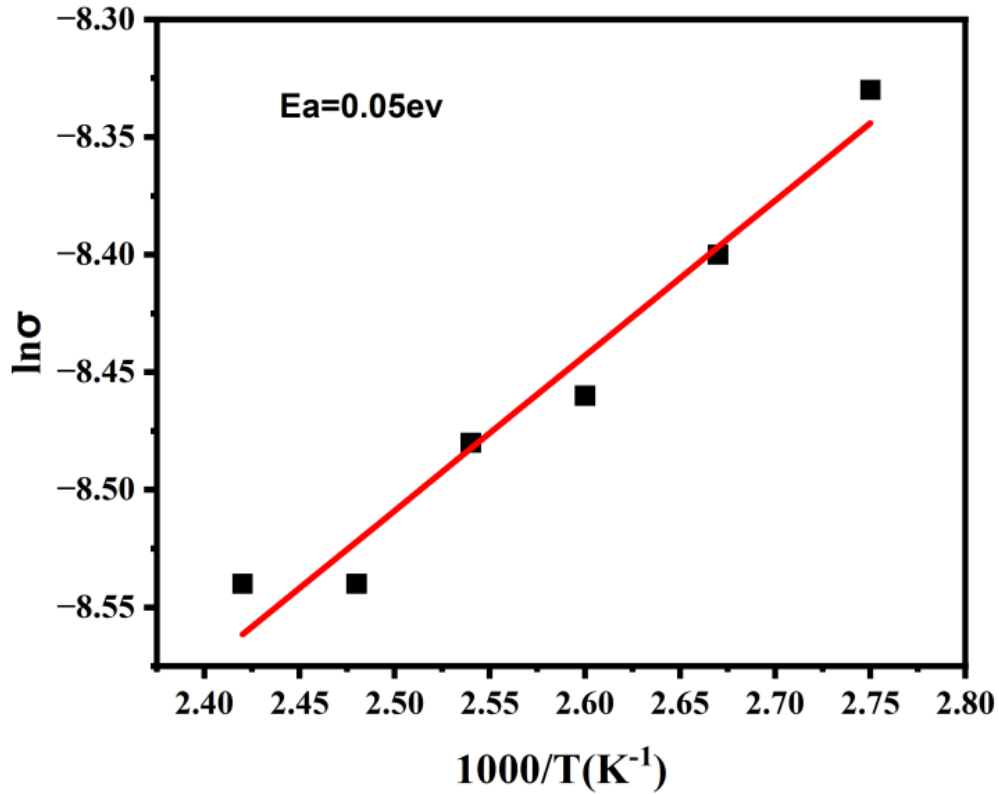


Figure 4.10 Arrhenius plot of ionic conductivity of LASO sample

A straight line in the figure 4.10 indicates that the process Follows Arrhenius behavior. The activation energy was estimated to be 0.05eV. The $E_a = 0.05\text{eV}$ indicate low energy barrier, likely indicating fast ionic or electronic transport. Activation energy and ionic conductivity has a strong correlation between them as the activation energy decreases ionic conductivity increases while at the same time it has been seen that the Li^* diffusibility increases across the material due to lower in activation energy, high diffusibility of ions may enhance the cyclability of solid-state battery.

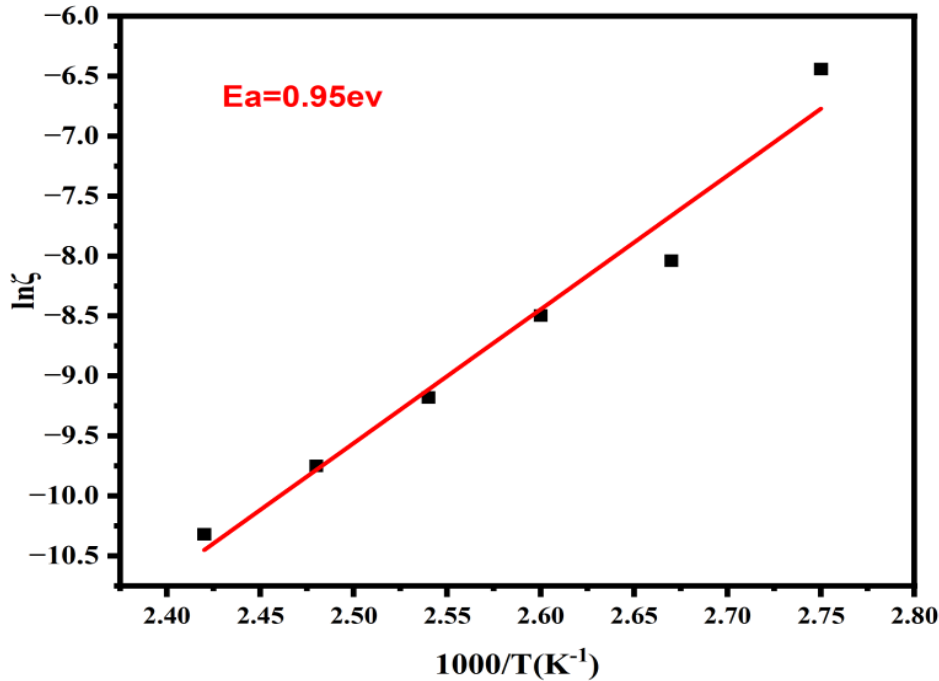


Figure 4.11 Arrhenius representation of relaxation time versus temperature for sample LASO

The graphical representation (Figure 4.11) showing relaxation time (τ) against temperature obtained from Nyquist plot analysis offers understanding of thermal activation mechanisms in relaxation phenomena within materials. Relaxation time is determined using peak frequency (f_{\max}) from Nyquist plots through the relationship $\tau = 1/2\pi f_{\max}$. The thermal dependency of τ typically exhibits an Arrhenius-type behavior: $\tau = \tau_0 \exp(E_a/k_B T)$, where τ_0 signifies the pre-exponential factor, T indicates absolute temperature, and E_a represents the activation energy. This relationship demonstrates that relaxation time undergoes exponential reduction with rising temperature, as elevated thermal energy facilitates accelerated relaxation mechanisms. When represented as $\ln(\tau)$ against $1/T$ (Arrhenius representation), the gradient of the linear relationship yields the activation

energy (E_a), which measures the thermal energy barrier for relaxation phenomena. An activation energy value of 0.96eV indicates a moderate thermal barrier controlling relaxation dynamics.

5

SUMMARY AND CONCLUSIONS

The LASO solid electrolyte was synthesized via a conventional solid-state reaction technique. The optimum conditions of phase formation, sintering temperature, and weight loss were identified by using TGA and DSC up to 850 °C, wherein the first derivative of the weight loss curve provided ease in its assessment. TGA results indicated a cumulative weight loss of approximately 21% up to 850 °C. X-ray diffraction (XRD) analysis showed that the optimal sintering temperature for forming LiAlSiO₄ based solid electrolytes is 1000 °C and verified the formation of the hexagonal LASO phase. At temperatures below 1000 °C, XRD patterns revealed the existence of a LiAlO₂ impurity phase, which was eliminated by sintering at elevated temperatures. Dielectric analysis reflected Maxwell–Wagner relaxation behavior, wherein the dielectric constants ϵ' and ϵ'' changed with frequency. The impedance spectroscopy showed downpressed semicircles, which are due to grain boundary contributions in the relaxation process, and this further establishes the Maxwell–Wagner relaxation mechanism.

REFERENCES

1. Luo X, Wang J, Dooner M, Clarke J. Overview of current development in electrical energy storage technologies and the application potential in power system operation. *Appl Energy* 2015; 137: 511–536.
2. Cloete S, Arnaiz del Pozo C, Jiménez Álvaro Á. System-friendly process design: Optimizing blue hydrogen production for future energy systems. *Energy* 2022; 259.
3. Jaccard M. Sustainable Fossil Fuels: The Unusual Suspect in the Quest for Clean and Enduring Energy. *Sustainable Fossil Fuels: The Unusual Suspect in the Quest for Clean and Enduring Energy* 2006; 1–381.
4. Nagmani, Debanjana Pahari, Ashwani Tyagi, Dr. Sreeraj Puravankara. Lithium-Ion Battery Technologies for Electric Mobility – State-of-the-Art Scenario. *ARAI Journal of Mobility Technology* 2022; 2: 233–248.
5. Learn About Batteries - Battery University. <https://batteryuniversity.com/articles> (8 June 2025, date last accessed).
6. Zhang M, Song X, Ou X, Tang Y. Rechargeable batteries based on anion intercalation graphite cathodes. *Energy Storage Mater* 2019; 16: 65–84.
7. Long Y, Shu Y, Ma X, Ye M. In-situ synthesizing superior high-rate LiFePO₄/C nanorods embedded in graphene matrix. *Electrochim Acta* 2014; 117: 105–112.
8. Kabir MM, Demirocak DE. Degradation mechanisms in Li-ion batteries: a state-of-the-art review. *Int J Energy Res* 2017; 41: 1963–1986.
9. Zhang B, Tan R, Yang L *et al.* Mechanisms and properties of ion-transport in inorganic solid electrolytes. *Energy Storage Mater* 2018; 10: 139–159.
10. Jie Y, Ren X, Cao R, Cai W, Jiao S. Advanced Liquid Electrolytes for Rechargeable Li Metal Batteries. *Adv Funct Mater* 2020; 30: 1910777.
11. Zhang Z, Zhang Q, Ren C *et al.* A ceramic/polymer composite solid electrolyte for sodium batteries. *J Mater Chem A Mater* 2016; 4: 15823–15828.
12. Nzereogu PU, Oyesanya A, Ogba SN *et al.* Solid-State lithium-ion battery electrolytes: Revolutionizing energy density and safety. *Hybrid Advances* 2025; 8: 100339.
13. Yaroshevsky AA. Abundances of chemical elements in the Earth's crust. *Geochemistry International* 2006; 44: 48–55.

14. Fleischer M. The abundance and distribution of the chemical elements in the earth's crust. *J Chem Educ* 1954; 31: 446–455.
15. Sheil R, Perng YC, Mars J *et al.* Synthesis and Crystallization of Atomic Layer Deposition β -Eucryptite LiAlSiO_4 Thin-Film Solid Electrolytes. *ACS Appl Mater Interfaces* 2020; 12: 56935–56942.
16. Cho SJ, Uddin MJ, Alaboina P. Review of Nanotechnology for Cathode Materials in Batteries. *Emerging Nanotechnologies in Rechargeable Energy Storage Systems* 2017; 83–129.
17. Epp J. X-ray diffraction (XRD) techniques for materials characterization. *Materials Characterization Using Nondestructive Evaluation (NDE) Methods* 2016; 81–124.
18. De Assumpção Pereira-da-Silva M, Ferri FA. Scanning Electron Microscopy. *Nanocharacterization Techniques* 2017; 1–35.
19. mp-558713: LiAlSiO_4 (hexagonal, P6₂₂, 180). <https://legacy.materialsproject.org/materials/mp-558713/> (18 May 2025, date last accessed).
20. Ross S, Welsch AM, Behrens H. Lithium conductivity in glasses of the Li_2O – Al_2O_3 – SiO_2 system. *Physical Chemistry Chemical Physics* 2014; 17: 465–474.
21. Fan H, Zhang Y, Ding S. Ultra-low ϵ_r in LiAlSiO_4 microwave ceramics with Li excess. *J Alloys Compd* 2025; 1010: 177848.
22. Liu H, Azimi G. Process analysis and study of factors affecting the lithium carbonate crystallization from sulfate media during lithium extraction. *Hydrometallurgy* 2021; 199: 105532.
23. Xue W, Yang Q, Li S *et al.* The effect of LiAlSiO_4 additions on lithium ionic conductivity of garnet $\text{Li}_{6.75}\text{La}_3\text{Zr}_{1.75}\text{Nb}_{0.25}\text{O}_{12}$ prepared by solid-state synthesis. *Solid State Ion* 2020; 350: 115313.
24. Ding S, Yao X, Zhang LY, Mao Y. Microwave Dielectric Properties of $\text{Bi}_{1-x}\text{Li}_x\text{NbO}_4$ Ceramics. *Ferroelectrics* 2005; 327: 63–68.
25. Wang Q, Puntambekar A, Chakrapani V. Gaseous Reactions in Adsorbed Water Present on Transition Metal Oxides. *Journal of Physical Chemistry C* 2017; 121: 13151–13163.
26. Davaasuren B, Tietz F. Impact of sintering temperature on phase formation, microstructure, crystallinity and ionic conductivity of $\text{Li}_{1.5}\text{Al}_{0.5}\text{Ti}_{1.5}(\text{PO}_4)_3$. *Solid State Ion* 2019; 338: 144–152.

27. Jadaun SS, Panwar AK, Geetanjali. Effects of heterogeneous structure on conduction mechanism and electrochemical performance of LiTa₂PO₈-fast lithium-ion conductor in quasi-solid-state lithium-ion batteries. *J Energy Storage* 2025; 115: 116030.
28. Irshad M, Rafique M, Tabish AN *et al.* Influence of Sintering Temperature on the Structural, Morphological, and Electrochemical Properties of NiO-YSZ Anode Synthesized by the Autocombustion Route. *Metals* 2022, Vol 12, Page 219 2022; 12: 219.
29. Xu H, Heaney PJ, Beall GH. Phase transitions induced by solid solution in stuffed derivatives of quartz: A powder synchrotron XRD study of the LiAlSiO₄-SiO₂ join. *American Mineralogist* 2000; 85: 971–979.
30. Wiedemann D, Nakhal S, Rahn J *et al.* Unravelling Ultraslow Lithium-Ion Diffusion in γ -LiAlO₂: Experiments with Tracers, Neutrons, and Charge Carriers. *Chemistry of Materials* 2016; 28: 915–924.
31. He X, Bai Q, Liu Y, Nolan AM, Ling C, Mo Y. Crystal Structural Framework of Lithium Super-Ionic Conductors. *Adv Energy Mater* 2019; 9: 1902078.
32. Jadaun SS, Panwar AK, Geetanjali. The Effect of Multi-step Sintering on the density of Li₇La₃Zr_{1.75}Ce_{0.25}O₁₂ as Solid State Electrolyte Material. *Indian Journal of Pure & Applied Physics (IJPAP)* 2024; 62: 116–123.
33. Meena R, Dhaka RS. Dielectric properties and impedance spectroscopy of NASICON type Na₃Zr₂Si₂PO₁₂. *Ceram Int* 2022; 48: 35150–35159.
34. Nallamuthu N, Prakash I, Satyanarayana N, Venkateswarlu M. Electrical conductivity studies of nanocrystalline lanthanum silicate synthesized by sol–gel route. *J Alloys Compd* 2011; 509: 1138–1145.
35. West AR, Adams TB, Morrison FD, Sinclair DC. Novel high capacitance materials:- BaTiO₃:La and CaCu₃Ti₄O₁₂. *J Eur Ceram Soc* 2004; 24: 1439–1448.
36. Yang CF. Improvement of the sintering and dielectric characteristics of surface barrier layer capacitors by CuO addition. *Japanese Journal of Applied Physics, Part 1: Regular Papers and Short Notes and Review Papers* 1996; 35: 1806–1813.
37. Yang J, Bai W, Zhang Y, Jonscher AK, Holloway R. Dielectric relaxation in solids. *J Phys D Appl Phys* 1999; 32: R57.
38. Impedance Spectroscopy: Theory, Experiment, and Applications. https://www.researchgate.net/publication/271768109_Impedance_Spectroscopy_Theory_Experiment_and_Applications (18 May 2025, date last accessed).

PLAGIARISM REPORT

Thesis Parul Solanki(2k23_MSCPHY_38),Ayushi sharma(2k23_MSCPHY_90)

Delhi Technological University

Document Details

Submission ID

trn:old:::27535:99733270

Submission Date

Jun 7, 2025, 11:06 AM GMT+5:30

Download Date

Jun 7, 2025, 11:08 AM GMT+5:30

File Name

THESIS REPORT 7JUNE 2025 final.docx

File Size

3.7 MB

41 Pages

8,668 Words

52,907 Characters





8% Overall Similarity

The combined total of all matches, including overlapping sources, for each database.




Filtered from the Report

- Bibliography
- Quoted Text
- Cited Text
- Small Matches (less than 10 words)

Match Groups

-  **58 Not Cited or Quoted 8%**
Matches with neither in-text citation nor quotation marks
-  **0 Missing Quotations 0%**
Matches that are still very similar to source material
-  **0 Missing Citation 0%**
Matches that have quotation marks, but no in-text citation
-  **0 Cited and Quoted 0%**
Matches with in-text citation present, but no quotation marks

Top Sources

- 2%  Internet sources
- 5%  Publications
- 2%  Submitted works (Student Papers)

LIST OF CONFERENCES

Name of Conference: 3rd International Conference on Advanced Functional Materials and Devices for sustainable development (AFMD-2025)

Conference Dates: 2025, March 03-05

Mode of the conference: Offline

Venue: Department of Physics and Internal Quality Assurance Cell (IQAC) of Atma Ram Sanatan Dharma College, University of Delhi

Name of Conference: International Conference on Advanced Materials for Sustainable Future (ICAMSF-2025).Conference

Dates: 2025, March 28-29

Mode of the conference: Offline

Venue: Chitkara University, Punjab.

1st CONFERENCE RECORD

PROOF OF REGISTRATION



PAYMENT RECEIPT



₹1,000.00

Paid to Gyantosh Jha

UPI ID: atmaramsantan@icici

20 February 2025, 6:51 pm

UPI transaction ID: 505172669212

PARTICIPATION CERTIFICATES



ATMA RAM SANATAN DHARMA COLLEGE
UNIVERSITY OF DELHI
Accredited Grade 'A++' By NAAC || All India 5th Rank in NIRF (Ministry of Education)
3rd International Conference on
Advanced Functional Materials and Devices (AFMD-2025)
for Sustainable Development
Under the aegis of IQAC and supported by Department of Biotechnology (GoI)

Certificate of Participation
This is to certify that Prof./Dr./Mr./Ms.
PARUL SOLANKI
DELHI TECHNOLOGICAL UNIVERSITY
has participated in the 3rd International Conference on "Advanced Functional Materials & Devices for Sustainable Development" (AFMD-2025) organised by Department of Physics under the aegis of IQAC ARSD College, University of Delhi, India during March 03-05, 2025 in hybrid mode.
He/She has presented **Poster** entitled:
PP-31:-Study of XRD, dielectric properties and ionic conductivity of Li-Ai-Si-O₄ ceramic solid electrolyte synthesized by solid state method


Dr. Shankar Subramanian
Convener, AFMD-2025


Dr. Anjali Sharma
Convener, AFMD-2025


Prof. Vinita Tuli
Coordinator, IQAC


Prof. Gyantosh Kumar Jha
Principal/Patron AFMD-2025

Certificate No: ARSD/AFMD25/PP/031

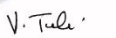


ATMA RAM SANATAN DHARMA COLLEGE
UNIVERSITY OF DELHI
Accredited Grade 'A++' By NAAC || All India 5th Rank in NIRF (Ministry of Education)
3rd International Conference on
Advanced Functional Materials and Devices (AFMD-2025)
for Sustainable Development
Under the aegis of IQAC and supported by Department of Biotechnology (GoI)

Certificate of Participation
This is to certify that Prof./Dr./Mr./Ms.
AYUSHI SHARMA
DELHI TECHNOLOGICAL UNIVERSITY
has participated in the 3rd International Conference on "Advanced Functional Materials & Devices for Sustainable Development" (AFMD-2025) organised by Department of Physics under the aegis of IQAC ARSD College, University of Delhi, India during March 03-05, 2025 in hybrid mode.
He/She has presented **Poster** entitled:
PP-08:-Study of XRD, dielectric properties and ionic conductivity of Li-Ai-Si-O₄ ceramic solid electrolyte synthesized by solid state method


Dr. Shankar Subramanian
Convener, AFMD-2025


Dr. Anjali Sharma
Convener, AFMD-2025


Prof. Vinita Tuli
Coordinator, IQAC


Prof. Gyantosh Kumar Jha
Principal/Patron AFMD-2025

Certificate No: ARSD/AFMD25/PP/008

2nd CONFERENCE RECORD

PROOF OF REGISTRATION

PAYMENT RECEIPT



(<https://www.chitkara.edu.in/>)

International Conference on Advanced Materials Sustainable Future (ICAMSF-2025)

(<https://www.chitkara.edu.in/>)

Dear PARUL SOLANKI,

Please check your transaction details below:

Reg. Date	15-MAR-2025
Online Id	ICAMSF0653
Payment Id	250315221917237
Payable Amount	Rs. 5000
Payment Status	Success
Name	PARUL SOLANKI
Email	parulrajput1f@gmail.com
Contact No.	+917017003454
Paper ID	495
Paper Title	Impact of Sintering Temperature on Conductivity and Electrochemical Properties of LiAlSiO ₄ as Solid-State Electrolyte for Li-ion batteries
Accommodation	Yes
Category	Student/Research Scholar
User Type	Participants

PARTICIPATION CERTIFICATES



PROOF OF SUBMISSION

Research Article

Structural and dielectric investigation of LiAlSiO₄ ceramic solid electrolyte synthesized by solid state route

Submission ID f6ee8b09-6d50-4f9f-a837-2f8109d9705b

Submission Version Initial Submission

PDF Generation 08 Jun 2025 13:30:45 EST by Atypon ReX

Authors

Ayushi Sharma

Affiliations

- Department of Applied Physics, Delhi Technological University, Delhi-110042, India

Parul Solanki

Affiliations

- Department of Applied Physics, Delhi Technological University, Delhi-110042, India

Sharad Singh Jadaun

Affiliations

- Department of Applied Physics, Delhi Technological University, Delhi-110042, India

Amrish K Panwar
Corresponding Author
Submitting Author



<https://orcid.org/0000-0002-1694-7261>

Affiliations

- Department of Applied Physics, Delhi Technological University, Delhi-110042, India
-

SCOPUS INDEXING



Edited By: Amit Bandyopadhyay

Online ISSN: 1744-7402

Print ISSN: 1546-542X

© 2025 The American Ceramic Society

ACT reports ceramic technology, engineering, modelling and process research that moves ceramics and composites from lab to production.



Latest issue

Volume 22, Issue 4
July/August 2025

[HOME](#) [FOR AUTHORS](#) [ARTICLES](#) [COLLECTIONS](#) [ABOUT](#)



International Journal of Applied Ceramic Technology publishes applied research on how ceramics and composites are developed for use in the commercial world. This ceramic engineering journal focuses on the commercialization of engineered ceramics, products and processes.

Journal Metrics

3.8
CiteScore

1.8
Journal Impact
Factor

41%
Acceptance Rate

29 days
Submission To First
Decision

Sign up for email alerts

Enter your email to receive alerts when new articles and issues are published.

Email address

Enter email

Activate Windows
Go to Settings to activate Windows.

Continue